Quantum statistics control with a plasmonic nanocavity: Multimode-enhanced interferences

Dongxing Zhao,[1] Ying Gu,[1,2,*] Hongyi Chen,[1] Juanjuan Ren,[1] Tiancai Zhang,[3] and Qihuang Gong[1,2]

[1]*State Key Laboratory for Mesoscopic Physics, Department of Physics, Peking University, Beijing 100871, China*
[2]*Collaborative Innovation Center of Quantum Matter, Beijing, China*
[3]*State Key Laboratory of Quantum Optics and Quantum Optics Devices, Institute of Opto-Electronics,*
Shanxi University, Taiyuan 030006, China

Using a scattered field interference mechanism, we theoretically demonstrate the quantum statistics control with a hybrid system comprised of a quantum emitter and a plasmonic multimode nanocavity. Enhanced through multimode interactions, destructive interference between scattered fields from the emitter and nanocavity is able to change the photon statistics from bunching to antibunching. This transition cannot be explained by treating the plasmonic nanocavity in the dipole approximation. In some specific regions, an effective single-mode model, which is equivalent to the multimode model, is derived by simply shifting the transition frequency and modifying decay rates of the nearby quantum emitter. Superior to the closed optical microcavity, this hybrid system can be used to control the photon statistics without the need for strong coupling, and may find applications in nanoscale refractive index sensing.

PACS number(s): 42.50.Pq, 42.82.Fv, 78.67.Bf, 42.50.Ar

I. INTRODUCTION

The coherent control of quantum statistics forms an important part of quantum-optical spectroscopy [1–5]. Various schemes based on the cavity quantum electrodynamics (CQED) system have been proposed to tune the photon statistics [6–12], such as antibunched and bunched output fields generated with photon blockade and photon-induced tunneling effects [6–11], and all-optical control of quantum statistics using cavity electromagnetically induced transparency [12]. However, most of these schemes rely on strong coupling, which raises certain difficulties for practical application. Furthermore, conventional optical cavities are usually micrometers in size, which is not favorable for scalable and ultracompact integration.

A good candidate to overcome these limitations is the metallic nanocavity, where collective electron oscillations enable the enhancement and confinement of light at the nanoscale [13,14]. The hybridization of a quantum emitter (QE) and a metallic nanoparticle (MNP) can yield functionalities that exceed those of the individual subunits [15,16], including Fano resonance [17] and its effect on quantum statistics [18], tailored spontaneous emission [19,20], spaser [21–23], enhanced up-conversion of entangled photons [24], cloaking [25], and the generation of squeezed states [26]. Generally, the MNP can be viewed as an open nanocavity. This openness leads to interference between scattered fields from QE and MNP.

Here, with a plasmonic multimode nanocavity, we describe using this scattered field interference to control the photon statistics. Besides having an ultrasmall mode volume, there are several advantages to using this cavity, one being high openness. The incident light then couples to both the QE transition and MNP modes and, therefore, both scatter the incident light. Subsequent constructive or destructive interference between the scattered fields leads to various photon statistics. Another advantage is that the MNP is a multimode

cavity with spectral overlap among its modes. If the QE and MNP are several nanometers apart, multimode effects must be taken into account. Beyond the dipole approximation [18], the coupling between QE and higher modes further enriches the properties of the photon statistics. Third, the multimode interactions and openness-induced photon interferences can boost the tunability of photon statistics even if the coupling of QE and MNP is in the bad-cavity limit.

Without loss of generality, we consider the simplest QE-MNP system composed of a two-level QE and spherical MNP to capture the main physics. The theoretical model can also be applied to the more complex-shaped MNP. As for the more complex-shaped MNP, such as nanorod or bipyramid, they also possess the dipole mode, quadruple mode, and so on. Their interactions with nearby QE can also be described by the following theoretical model. To obtain the corresponding system response parameters (e.g., resonance frequency and coupling constant), electromagnetic simulations are needed [27,28]. To give an exact description of this system, we develop a full quantum model where the MNP is treated as a multimode cavity. It is shown that the dipole approximation [18] fails to describe the quantum statistical properties of this hybrid system when QE is close to MNP. In some specific parameter regions, we deduce an effective single-mode model, which greatly simplifies the numerical calculations and fits well with the multimode model. This effective model provides a clear physical picture, where the role of the higher modes is to modify the QE transition frequency and decay rate only. By changing the frequency of the incident light, the distance between the QE and MNP, and the background permittivity, both bunched and antibunched fields can be obtained through the interference of scattered lights. The hybrid QE-MNP system thus provides a unique method to manipulate the quantum statistics at the nanoscale.

This paper is organized as follows. In Sec. II, we set up the quantum multimode model of the hybrid system. The roles of multimode interactions and field interference on the photon statistics are analyzed in Sec. III. To obtain a clearer

*ygu@pku.edu.cn

033836-1

physical picture of the multimode interactions, we derive in Sec. IV an effective model by adiabatically eliminating the higher-mode operators of MNP. The photon statistics control by system parameters is explored in Sec. V. Finally, we present a discussion and summary in Sec. VI.

II. QUANTUM MULTIMODE MODEL

The system under study [Fig. 1(a)] consists of a two-level QE and spherical MNP with radius r_m and dielectric constant ε_m. The QE and MNP are separated by distance R and embedded in a dielectric host with permittivity ε_b. The whole system is driven by an applied field $E_0(e^{-i\omega t} + e^{i\omega t})$. The MNP is able to support localized electromagnetic modes, known as surface plasmon resonances [14]. For a spherical MNP much smaller than the wavelength of incident light, the resonance frequency ω_n of its nth mode is determined by $\mathrm{Re}[\varepsilon_m(\omega_n)] = -\frac{n+1}{n}\varepsilon_b$ ($n = 1, 2, 3, \ldots$) [29]. From the experimental data [30] for ε_m, the modes of a silver MNP in vacuum ($\varepsilon_b = 1$) overlap with each other [Fig. 1(b), in which only the first five modes are shown]. The dipole mode ($n = 1$) can be excited by an incident plane wave and can radiate to the far field. If the MNP is small enough, the higher modes [such as quadruple ($n = 2$) and octuple ($n = 3$) modes] cannot couple to the incident light because of their vanishing dipole moments [31,32], but they can be excited by nearby dipoles [31]. If distance R is small, we must consider the coupling of QE with the higher modes of MNP due to the mode overlap.

In a frame rotating at the incident light frequency ω, the interaction Hamiltonian of the hybrid system within the rotating-wave approximation reads ($\hbar = 1$)

$$H = (\omega_x - \omega)\sigma^\dagger\sigma + \sum_{n=1}^{N}(\omega_n - \omega)a_n^\dagger a_n$$

$$- \sum_{n=1}^{N} g_n(a_n\sigma^\dagger + a_n^\dagger\sigma) - E_0\chi(a_1 + a_1^\dagger) - \mu E_0(\sigma + \sigma^\dagger).$$

$$(1)$$

The first two terms are the free Hamiltonian for QE and MNP, with a_n being the annihilation operator of the nth mode of MNP; $\sigma = |g\rangle\langle e|$ is the lowering operator of QE, with $|g\rangle$ ($|e\rangle$) being the ground (excited) state; and ω_x and ω_n denote the resonance frequency of the QE and nth mode of MNP, respectively. For the system parameters discussed in the following, 15 modes ($N = 15$) have been taken into consideration, which guarantee convergence and can represent the steady-state results of $N \to \infty$. The middle term describes the interaction between QE and MNP, where $g_n = \frac{\mu(n+1)}{R^{n+2}}\sqrt{\frac{2n+1}{n}\frac{\eta_n r_m^{2n+1}}{4\pi\varepsilon_0}}$ is the coupling constant between the nth mode of MNP and QE, with $\eta_n = 1/\frac{d}{d\omega}\mathrm{Re}[\varepsilon_m(\omega)]|_{\omega=\omega_n}$ and dipole moment μ of QE. The coupling constant g_n is obtained through a classical-quantum correspondence approach. This is achieved by comparing the classical electromagnetic results of MNP polarization fields acting on QE, which are composed of the near field excited by E_0 and the feedback field from MNP, with the quantum results $\langle E_m^+\rangle = \sum_{n=1}^{N}\frac{g_n}{\mu}\langle a_n\rangle$. Details of the derivation are provided in Appendix A. The last two terms, originating from the high openness of the metallic nanocavity, represent the driving of the QE and MNP dipole mode by the applied field, with $\chi = \varepsilon_b\sqrt{12\pi\varepsilon_0\eta_1 r_m^3}$ being the dipole moment of MNP (see Appendix A). As a comparison, an incident light drives either the cavity mode or the QE in a conventional CQED system. We show below that by introducing the unique interference effects caused by the high openness of the metallic nanocavity, the multimode couplings between QE and MNP can improve the performance on the control of photon statistics.

The dynamics of the system is given by the master equation

$$\dot{\rho} = i[\rho, H] + \frac{\gamma_x}{2}(2\sigma\rho\sigma^\dagger - \sigma^\dagger\sigma\rho - \rho\sigma^\dagger\sigma)$$

$$+ \sum_{n=1}^{N}\frac{\gamma_n}{2}(2a_n\rho a_n^\dagger - a_n^\dagger a_n\rho - \rho a_n^\dagger a_n), \quad (2)$$

where γ_x and γ_n are the decay rates of the QE and nth mode of the MNP, with $\gamma_n = 2\eta_n\mathrm{Im}[\varepsilon_m(\omega_n)]$ [21]. Although the possibility of strong coupling between single QE and MNP has been theoretically demonstrated [33], here we focus on the bad-cavity limit, i.e., $g_n < \gamma_n$ [see Fig. 1(c) for the first three modes]. This focus covers the general case for the hybrid QE-MNP system and is easier to achieve experimentally. The Hamiltonian [Eq. (1)] can also be extended to the strong-coupling regime [28,34], where the reversible energy exchange between QE and MNP takes place. Starting with the master equation, we can solve the populations and higher-order correlation functions for the steady state. For this purpose, one needs to truncate the Fock basis of the MNP modes according to both the driven strength E_0 and the coupling strength g_n. The general coupled equations for the hybrid system are presented
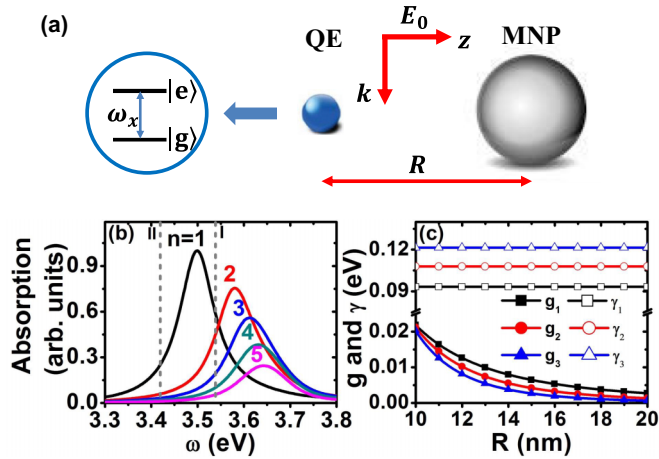

FIG. 1. (Color online) (a) Schematic of the hybrid system composed of a two-level QE and a spherical MNP. The whole system is driven by a plane wave. (b) Energy absorption of a silver MNP in vacuum contributed by its dipole mode ($n = 1$), quadruple mode ($n = 2$), and octuple mode ($n = 3$), etc. The vertical dashed lines show the QE frequencies discussed in the main text, including $\omega_x = 3.54$ eV (case I) and $\omega_x = 3.42$ eV (case II). (c) The coupling rate g_n (curves with solid symbol) and decay rate γ_n (curves with hollow symbol) with respect to distance R for the nth ($n = 1, 2, 3$) modes of MNP.

in Appendix B. The results of the calculations below are also verified using the open-source software QuTiP [35,36].

III. ROLE OF MULTIMODE INTERACTIONS AND FIELD INTERFERENCE

In the following, we calculate the second-order correlation function $g^{(2)}(0)$ of the scattered light. Because of the high openness of the nanocavity, both the MNP and QE scatter incident light. Hence, the total polarization operator is $\hat{P} = \chi a_1 + \mu \sigma$ [18]. Because their dipole moments vanish, the higher modes cannot scatter the light into the far field, and hence they are not included in the total polarization operator. For this hybrid system, the scattered intensity is proportional to $I = \langle \hat{P}^\dagger \hat{P} \rangle$, while the second-order correlation function is given by $g^{(2)}(0) = \langle (\hat{P}^\dagger)^2 (\hat{P})^2 \rangle / I^2$. The fields scattered from QE and MNP interfere with each other, which can be used to control the quantum statistics.

To gain a more physical understanding of the cavity-openness-induced interference, $g^{(2)}(0)$ can be rewritten in the following form:

$$g^{(2)}(0) = \chi^4 \langle (a_1^\dagger)^2 a_1^2 \rangle / I^2 + 4\chi^2 \mu^2 \langle a_1^\dagger a_1 \sigma^\dagger \sigma \rangle / I^2 + 4\chi^3 \mu \mathrm{Re} \langle a_1^\dagger a_1^2 \sigma^\dagger \rangle / I^2. \quad (3)$$

The positive semidefiniteness of the $(a_1^\dagger)^2 a_1^2$ and $a_1^\dagger a_1 \sigma^\dagger \sigma$ guarantees that the expectations in the first two terms of $g^{(2)}(0)$ are always non-negative. However, the third term in Eq. (3) can be positive or negative, which introduces
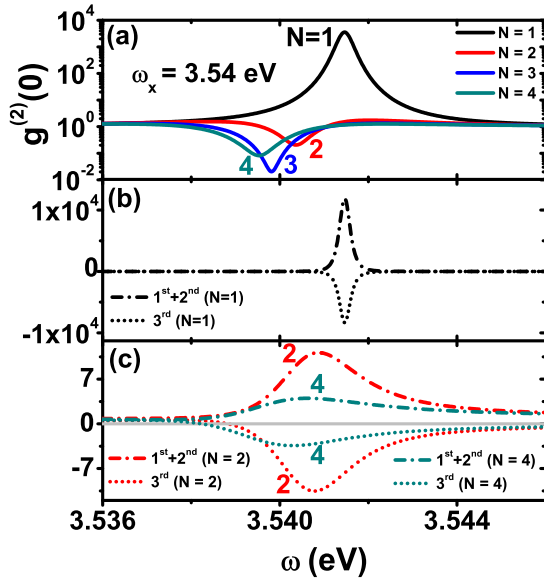
either constructive or destructive interference into the quantum statistics. This particular interference mechanism derives from the high openness of the plasmonic nanocavity.

We first illustrate the influence of the higher modes on the quantum statistics of scattered fields. From here on, the radius of the silver MNP is set to $r_m = 7$ nm. The dipole moment and decay rate of the QE in vacuum are set to $\mu = 0.7$ enm and $\gamma_x = 50$ μeV. The distance R is set to 12 nm, unless otherwise stated. A weak incident field with Rabi frequency $\Omega = 2\mu E_0 = 0.02$ meV is considered. Two typical QE transition frequencies, marked by two vertical lines in Fig. 1(b), were studied. For case I, the QE frequency is set to $\omega_x = 3.54$ eV, which lies between the dipole mode and other higher modes frequencies, whereas for case II, the QE is red detuned from the dipole mode with $\omega_x = 3.42$ eV. In Figs. 2(a) and 3(a), $g^{(2)}(0)$ is plotted for cases I and II, respectively. The photon statistics is reversed by the higher modes for case I [Fig. 2(a)]. In other words, the photon statistics of the scattered field is changed from bunching for $N = 1$ to antibunching because of multimode interactions. For case II, compared with the single-mode result, the multimode interactions shift the positions and magnitudes of the maximum and minimum of $g^{(2)}(0)$ [Fig. 3(a)]. In this case, by tuning the frequency of incident light, the character of the quantum statistics can either be bunching or antibunching.

In further analysis, the sum of the first two terms (dash-dotted curves) and the third term (dotted curves) in Eq. (3) are plotted separately in Figs. 2(b), 2(c), and 3(b). As already mentioned, the third term of $g^{(2)}(0)$ can be positive or negative for different frequencies, which yields constructive or destructive interference of quantum statistics. Figures 2(b) and 2(c) indicate that the statistical interferences between the
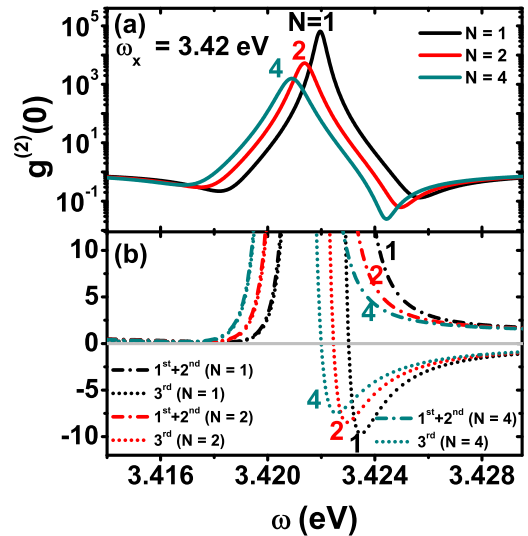

FIG. 2. (Color online) (a) Quantum statistics $g^{(2)}(0)$ of the scattered field as a function of incident light frequency ω for case I with $\omega_x = 3.54$ eV. Opposite quantum statistics characteristics are found due to the multimode interactions. Here, $N = 1$ means that we consider only the dipole mode, whereas $N = 2$ means that we consider both the dipole and quadruple modes; likewise for $N > 2$. (b) The sum of the first two terms (dash-dotted curves) and the third term (dotted curves) in Eq. (3) for $N = 1$. (c) Same as (b), but for $N = 2$ (red) and $N = 4$ (cyan). For $N > 1$, the destructive interference around the QE frequencies leads to antibunching statistics.

FIG. 3. (Color online) (a) Quantum statistics $g^{(2)}(0)$ as a function of incident light frequency ω for case II with $\omega_x = 3.42$ eV. The shift of the $g^{(2)}(0)$ curve induced by multimode interactions leads to a wider range of adjustment for the quantum statistics. (b) The sum of the first two terms (dash-dotted curves) and the third term (dotted curves) in Eq. (3) for $N = 1$ (black), $N = 2$ (red), and $N = 4$ (cyan). The interference of quantum statistics can be either constructive or destructive around QE frequencies.

scattered fields are mainly destructive around $\omega = \omega_x$ for case I. The magnitudes for both the sum of the first two terms and the third interference term decrease as N increases. In particular, for $N \geqslant 2$, the two curves in Fig. 2(c) have nearly the same magnitudes. However, the opposite sign of the third interference term reverses the photon statistics and leads to the antibunching effect. That is to say, the quantum statistics of the scattered field can go from bunching to antibunching under the destructive interference contributed by the multimode interactions. For case II, the statistical interference can be constructive or destructive [Fig. 3(b)]. The total effects of the multimode interactions and field interference are to shift the positions and magnitudes of the $g^{(2)}(0)$. Moreover, multimode interactions lead to a wider range of adjustment for quantum statistics than case I. For the cases that the QE is on resonance with the frequency of the dipole mode or one of the higher modes, poor tunability of the quantum statistics is found because only one of the modes of the MNP dominates the system.

The calculations above are based on the exact model [Eq. (1)] and the general dynamical equations given in Appendix B. This exact model reveals the role of multimode interactions to some degree. However, from Figs. 2(a) and 3(a), the steady-state results for $g^{(2)}(0)$ do not converge even if we take four modes ($N = 4$) into account. It is difficult to consider more than five or six modes because the corresponding density matrix is exceedingly large. This problem is even more severe for strong incident fields. To solve this problem, we derive in the next section a simplified single-mode model for this hybrid QE-MNP system.

IV. EFFECTIVE MODEL

By adiabatically eliminating the higher-mode operators a_i ($i \geqslant 2$) in Eq. (1), we develop an effective model which transforms the multimode problem into a single-mode problem. The adiabatic elimination is valid if the ratio of the coupling constants g_n to $|i(\omega_n - \omega_x) + (\gamma_n - \gamma_x)/2|$ is small. This effective model not only greatly saves on computation resources, but also helps to capture the physics clearly.

We start from the Heisenberg equations of motion for σ and a_n:

$$\dot{\sigma} = -\left[i(\omega_x - \omega) + \frac{\gamma_x}{2} \right]\sigma - \sum_{n=1}^{N} i g_n \sigma_z a_n - i\mu E_0 \sigma_z, \quad (4)$$

$$\dot{a}_n = -\left[i(\omega_n - \omega) + \frac{\gamma_n}{2} \right]a_n + i g_n \sigma + i E_0 \chi \delta_{n,1}, \quad (5)$$

where $\delta_{n,1}$ is the Kronecker delta. After some formal integrations and substitutions, an integral expression for $a_n(t)$ is obtained (see Appendix C). As an approximation, only the first-order terms with respect to $\frac{g_n}{i(\omega_n - \omega_x) + (\gamma_n - \gamma_x)/2}$ are retained. After dropping the fast rotating and decay terms, we obtain a simple approximation for $a_n(t)$ ($n \geqslant 2$):

$$a_n(t) \approx \frac{i g_n}{i(\omega_n - \omega_x) + (\gamma_n - \gamma_x)/2}\sigma(t) \quad (n \geqslant 2). \quad (6)$$

Substituting Eq. (6) into Eq. (4), and combining the obtained expression with the Heisenberg equation of a_1, the effective
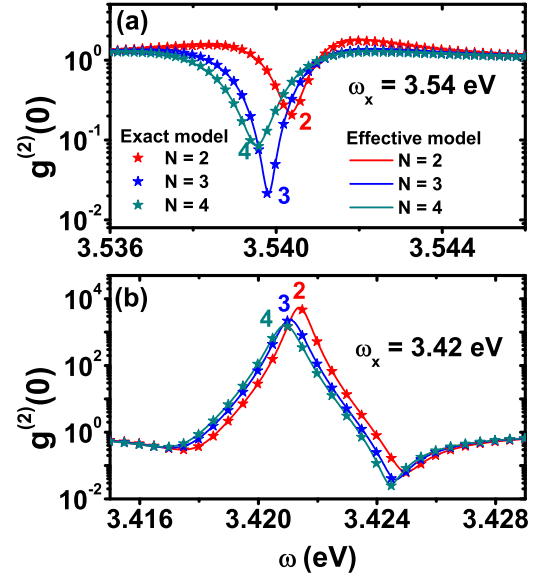

FIG. 4. (Color online) Comparison of $g^{(2)}(0)$ calculated from the effective model (solid curves) and exact model (solid stars) for (a) case I and (b) case II. Note the excellent match between the two models.

Hamiltonian is derived as

$$H_{\text{eff}} = (\omega_{x,\text{eff}} - \omega)\sigma^\dagger\sigma + (\omega_1 - \omega)a_1^\dagger a_1 - g_1(a_1\sigma^\dagger + a_1^\dagger\sigma)$$
$$- E_0\chi(a_1 + a_1^\dagger) - \mu E_0(\sigma + \sigma^\dagger), \quad (7)$$

and the corresponding effective master equation becomes

$$\dot{\rho}_{\text{eff}} = i[\rho_{\text{eff}}, H_{\text{eff}}] + \frac{\gamma_{x,\text{eff}}}{2}(2\sigma\rho_{\text{eff}}\sigma^\dagger - \sigma^\dagger\sigma\rho_{\text{eff}} - \rho_{\text{eff}}\sigma^\dagger\sigma)$$
$$+ \frac{\gamma_1}{2}(2a_1\rho_{\text{eff}}a_1^\dagger - a_1^\dagger a_1\rho_{\text{eff}} - \rho_{\text{eff}}a_1^\dagger a_1), \quad (8)$$

where the effective resonant energy $\omega_{x,\text{eff}}$ and decay rate $\gamma_{x,\text{eff}}$ of QE are modified as

$$\omega_{x,\text{eff}} = \omega_x - \sum_{n=2}^{N} \alpha_n(\omega_n - \omega_x),$$

$$\gamma_{x,\text{eff}} = \gamma_x + \sum_{n=2}^{N} \alpha_n(\gamma_n - \gamma_x), \quad (9)$$

with $\alpha_n = \frac{g_n^2}{(\omega_n - \omega_x)^2 + (\gamma_n - \gamma_x)^2/4}$. Equations (7)–(9) are the main results of the effective model. More details of the above derivations are given in Appendix C. From this effective Hamiltonian, the role of the higher modes is only to shift the QE resonance frequency and modify the decay rate, which enables the photon statistics to be controlled.

To verify the correctness of the effective model, comparisons of $g^{(2)}(0)$ between the exact model (solid stars) and the effective model (solid curves) were made (Fig. 4). Excellent matches are found between these two models for both cases. Because the spectral overlap among the modes of metallic nanostructures is general, the effective model thus provides an efficient way to treat multimode interactions. We point out that in the strong-coupling regime, this effective model is valid

only when the detunings between the QE and higher modes of MNP are large enough.

V. PHOTON STATISTICS CONTROL

In this section, we focus on the control of the photon correlation $g^{(2)}(0)$ via multimode effects of the MNP. In the following, the distance R between the QE and MNP is generally 10 to 20 nm, which does not satisfy the dipole approximation condition $R > 3r_m$ [37], so multimode effects must be considered. To guarantee the convergence of the steady-state results, at most 15 modes of the MNP are taken into account, which represents the $N \to \infty$ results.

We first tune the photon statistics of the scattered field by changing the frequency of the incident light. In the following, the QE frequency is set to $\omega_x = 3.42$ eV [case II in Fig. 1(b)]. By changing the frequency, we observe both bunching [$g^{(2)}(0) > 1$] and antibunching [$g^{(2)}(0) < 1$] photon statistics [Fig. 5(a)], which is the result of the coaction of all MNP modes. For example, at frequency $\omega \approx 3.421$ eV, a typical bunching effect is seen, whereas at $\omega \approx 3.424$ eV, a sharp dip in $g^{(2)}(0)$ appears, indicating strong photon antibunching. This antibunching character occurring in the bad-cavity limit is fundamentally different from that in a traditional CQED system, where the strong-coupling condition is necessary to control the photon statistics [6–11]. From the interference term [third term in Eq. (3)] caused by the high openness of the MNP plotted in Fig. 5(b), we can see that the statistical destructive interference leads to the sharp dip of $g^{(2)}(0)$.

For a fixed frequency of incident light, the quantum statistics of the scattered light can be controlled at the nanoscale. As the distance R decreases, the photon statistics makes a continuous transition from antibunching to bunching [Fig. 6(a)]. As shown in Fig. 6(b), the scattered intensity increases initially and then decreases with the QE and MNP

FIG. 6. (a) Second-order correlation $g^{(2)}(0)$ and (b) normalized scattered intensity with respect to the distance R when the incident light frequency is fixed at $\omega = 3.418$ eV. The intensity in (b) is normalized by the result of $R \to \infty$. The other parameters are the same as in Fig. 5.

getting closer. This intensity transition originates from the competing effects of near-field enhancement and nonradiative energy transfer from QE to MNP [38]. Compared with the scattering intensity of $R \to \infty$, enhanced scattered fields can be obtained for both bunched and antibunched light.

Finally, the properties of the photon statistics are also sensitive to the background permittivity ε_b. As indicated by the red solid curve in Fig. 7, the photon statistics can be switched from antibunching to bunching by increasing the permittivity. The control mechanism here can also be attributed to the interference induced by cavity openness. Moreover, setting the incident frequency to the dip frequency of $g^{(2)}(0)$ [$\omega \simeq 3.424$ eV; see Fig. 5(a)] provides a better option to control the photon statistics. Recall that the refractive index sensing in nanophotonics usually involves measuring
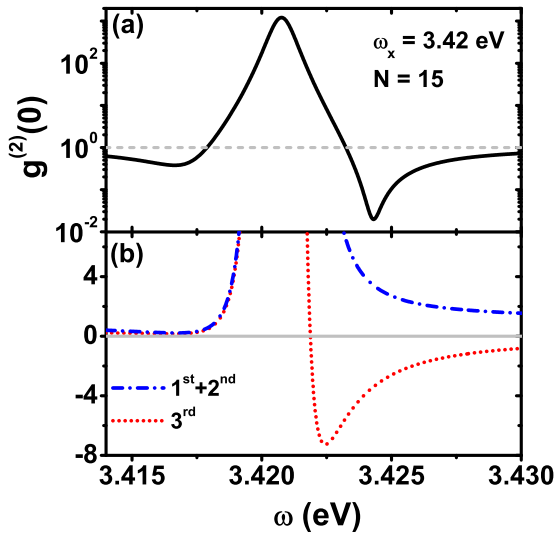
FIG. 5. (Color online) (a) Convergent multimode results ($N = 15$) for $g^{(2)}(0)$ calculated from the effective model for case II. The quantum statistics of the scattered field can be controlled by tuning the incident light frequency. (b) The sum of the first two terms (blue dash-dotted curve) and the third interference term (red dotted curve) in Eq. (3) for $N = 15$.
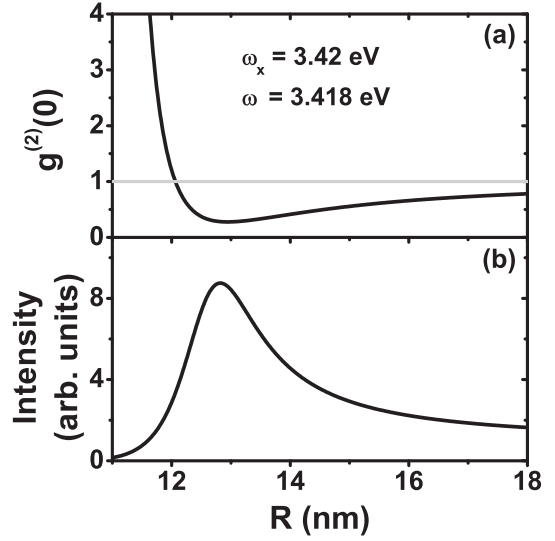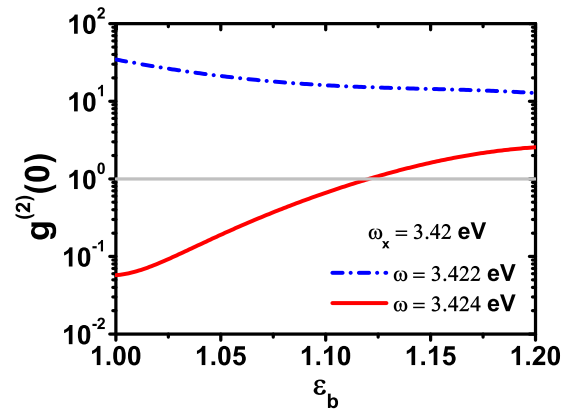
FIG. 7. (Color online) Second-order correlation function $g^{(2)}(0)$ with respect to the dielectric constant ε_b of background for $\omega = 3.422$ eV (blue dash-dotted curve) and $\omega = 3.424$ eV (red solid curve). The ε_b dependence of $g^{(2)}(0)$ provides insight into refractive index sensing. The other parameters are the same as in Fig. 5.

a shift of the surface plasmon resonance peak [39–41]. We emphasize that here the dependence of $g^{(2)}(0)$ on ε_b opens an alternative promising way. For practical applications, one prefers a strong signal from the coincidence measurement of the scattered field. This can be obtained in two ways. The first is increasing the scattered field intensity by using strong excitation and larger MNP with larger scattering cross section. The second way is improving the collection efficiency by using an optical nanofiber [42]. A designed nanoantenna which leads to directional emission can also help to boost the collection efficiency [43].

VI. DISCUSSION AND SUMMARY

We now discuss the experimental feasibility of the hybrid QE-MNP system. The QE can be a quantum dot [44], ultracold atom [45,46], molecule [47], ion [48], etc. As an example, a quantum dot coated with DNA and MNP can self-assemble [49,50] into an individual quantum dot-DNA-MNP complex. One can tune the distance between the QE and MNP by using different numbers of DNA bases [51]. With current developments in nanotechnology, scanning tunneling microscopes and atomic force microscopes can also be used to package the hybrid QE-MNP system [15]. The measurement of the second-order correlation function $g^{(2)}(0)$ can be performed by sending the scattered light to a Hanbury Brown–Twiss interferometer [52,53].

In conclusion, we have theoretically demonstrated that the hybrid QE-MNP system can execute nanoscale control of the quantum statistics of the scattered light field. Different from the conventional CQED methods, the control mechanism of quantum statistics is based on the scattering fields interference induced by high nanocavity openness. Moreover, a simple effective single-mode model has been derived, where the higher modes of the MNP modify the resonance frequency and decay rates of QE. We have obtained both bunched and antibunched fields by changing the frequency of the incident light, the distance between the QE and MNP, or the background dielectric constant. Thus, the dependence between the photon statistics and the background permittivity provides a promising path towards the refractive index sensing. The hybrid system can also be used as a building block for future nanophotonic quantum devices.

ACKNOWLEDGMENTS

APPENDIX A: DERIVATION OF COUPLING CONSTANTS

The Hamiltonian of the hybrid QE-MNP system in the Schrödinger picture is given by

$$H_S = \hbar\omega_x \sigma^\dagger \sigma + \sum_{n=1}^{N} \hbar\omega_n a_n^\dagger a_n - \mu(\sigma + \sigma^\dagger)\hat{E}_{\mathrm{MNP}}$$
$$- E(t)\chi(a_1 + a_1^\dagger) - \mu E(t)(\sigma + \sigma^\dagger), \quad \text{(A1)}$$

where σ is the lowering operator of QE, and a_n is the annihilation operator of the nth mode of MNP. $\hat{E}_{\mathrm{MNP}} = \sum_{n=1}^{N} \xi_n(a_n + a_n^\dagger)$ is the quantized electrical field of MNP acting on the QE with amplitude ξ_n, and $E(t) = E_0(e^{-i\omega t} + e^{i\omega t})$ represents the driven field. In addition, ω_x and ω_n are the resonance frequency of the QE and the nth mode of MNP; μ and χ denote the dipole moments of QE and MNP. Using the rotating-wave approximation and introducing $g_n = \mu\xi_n/\hbar$, the Hamiltonian can be rewritten as

$$H_S = \hbar\omega_x \sigma^\dagger \sigma + \sum_{n=1}^{N} \hbar\omega_n a_n^\dagger a_n - \sum_{n=1}^{N} \hbar g_n(a_n^\dagger \sigma + a_n \sigma^\dagger)$$
$$- E(t)\chi(a_1 + a_1^\dagger) - \mu E(t)(\sigma + \sigma^\dagger). \quad \text{(A2)}$$

After performing a unitary transformation $U = \exp[-i\omega(\sigma^\dagger\sigma + \sum_{n=1}^{N} a_n^\dagger a_n)t]$, we obtain the Hamiltonian H in the interaction picture,

$$H = i\hbar\dot{U}^\dagger U + U^\dagger H_S U$$
$$= \hbar(\omega_x - \omega)\sigma^\dagger\sigma + \sum_{n=1}^{N} \hbar(\omega_n - \omega)a_n^\dagger a_n$$
$$- \sum_{n=1}^{N} \hbar g_n(a_n\sigma^\dagger + a_n^\dagger\sigma) - E_0\chi(a_1 + a_1^\dagger)$$
$$- \mu E_0(\sigma + \sigma^\dagger). \quad \text{(A3)}$$

Starting from the master equation in the main text [Eq. (2)], the dynamics of the expectation values for arbitrary operator $\hat{F}$ can be given by

$$\frac{d}{dt}\langle\hat{F}\rangle = \frac{i}{\hbar}\langle[H,\hat{F}]\rangle + \frac{\gamma_x}{2}\langle[\sigma^\dagger,\hat{F}]\sigma + \sigma^\dagger[\hat{F},\sigma]\rangle$$
$$+ \sum_{n=1}^{N} \frac{\gamma_n}{2}\langle[a_n^\dagger,\hat{F}]a_n + a_n^\dagger[\hat{F},a_n]\rangle, \quad \text{(A4)}$$

with γ_x and γ_n denote the decay rates of the QE and nth mode of MNP. Next we consider the quantum mechanical result of the $\hat{E}_{\mathrm{MNP}}$ at the steady state. From Eq. (A4), the mean value dynamics of the field operator a_n is found to be

$$\frac{d}{dt}\langle a_n \rangle = -\left[i(\omega_n - \omega) + \frac{\gamma_n}{2}\right]\langle a_n \rangle + ig_n\langle\sigma\rangle + \frac{i}{\hbar}E_0\chi\delta_{1n},$$
$$\text{(A5)}$$

with δ_{1n} being the Kronecker delta. By using $d\langle a_n\rangle/dt = 0$, the resulting steady-state expectation of a_n is

$$\langle a_n \rangle_{\mathrm{ss}} = \frac{1}{i(\omega_n - \omega) + \frac{\gamma_n}{2}}\left(ig_n\langle\sigma\rangle + \frac{i}{\hbar}E_0\chi\delta_{1n}\right). \quad \text{(A6)}$$

Inserting the $\langle a_n \rangle_{\mathrm{ss}}$ into the positive frequency component of $\hat{E}_{\mathrm{MNP}}$ yields

$$\langle\hat{E}_{\mathrm{MNP}}^+\rangle_{\mathrm{ss}} = \sum_{n=1}^{N} \xi_n\langle a_n\rangle_{\mathrm{ss}}$$
$$= \frac{1}{\mu}\left[\frac{ig_1 E_0\chi}{i(\omega_1 - \omega) + \frac{\gamma_1}{2}} + \sum_{n=1}^{N} \frac{i\hbar g_n^2}{i(\omega_n - \omega) + \frac{\gamma_n}{2}}\langle\sigma\rangle\right]. \quad \text{(A7)}$$

This is the quantum mechanical result of $\hat{E}_{\mathrm{MNP}}$ with undetermined coupling constants g_n and dipole moment χ. From a classical electromagnetic view, the electrical field at the position of QE induced by the MNP polarization decomposes into two: one is the near field of the MNP excited by the applied field $E(t)$ and the other originates from the feedback that QE received from MNP. In other words, the MNP is polarized first by the QE. The polarization field of the MNP then reacts on the QE. Hence the classical electromagnetic result for E_{MNP}^+ can be represented as [54,55]

$$E_{\mathrm{MNP}}^+ = \frac{s_\alpha r_m^3}{R^3} \frac{\varepsilon_m(\omega) - \varepsilon_b}{\varepsilon_m(\omega) + 2\varepsilon_b} E_0$$
$$+ \sum_{n=1}^N \frac{s_n}{4\pi \varepsilon_0 \varepsilon_b} \frac{\varepsilon_m(\omega) - \varepsilon_b}{\varepsilon_m(\omega) + \frac{n+1}{n}\varepsilon_b} \frac{r_m^{2n+1}}{R^{2n+4}} \mu \langle \sigma \rangle, \quad (A8)$$

where r_m and $\varepsilon_m(\omega)$ denote the MNP radius and dielectric constant; R is the distance between QE and MNP; and s_α and s_n are the polarization parameters, with $s_\alpha = 2\,(-1)$ and $s_n = (n+1)^2\,[n(n+1)/2]$ for a radial (tangential) QE. The resonance frequency ω_n for the nth mode of MNP can be

determined from

$$\mathrm{Re}[\varepsilon_m(\omega_n)] = -\frac{n+1}{n}\varepsilon_b. \quad (A9)$$

Retaining just the first-order expansion of $\mathrm{Re}[\varepsilon_m(\omega)]$ around ω_n for the nth mode in Eq. (A8), we obtain

$$E_{\mathrm{MNP}}^+ = \frac{s_\alpha r_m^3}{R^3} \frac{i3\varepsilon_b\eta_1}{i(\omega_1 - \omega) + \frac{\gamma_1}{2}} E_0$$
$$+ \sum_{n=1}^N \frac{s_n}{4\pi \varepsilon_0 \varepsilon_b} \frac{i\frac{2n+1}{n}\varepsilon_b\eta_n}{i(\omega_n - \omega) + \frac{\gamma_n}{2}} \frac{r_m^{2n+1}}{R^{2n+4}} \mu \langle \sigma \rangle, \quad (A10)$$

where $\gamma_n = 2\eta_n \mathrm{Im}[\varepsilon_m(\omega_n)]$ is the decay rate of the nth mode of MNP [21], with $\eta_n = 1/\frac{d}{d\omega}\mathrm{Re}[\varepsilon_m(\omega)]|_{\omega=\omega_n}$. Comparing the classical electromagnetic [Eq. (A10)] and quantum mechanical [Eq. (A7)] results of E_{MNP}^+ yields expressions for g_n and χ:

$$g_n = \frac{\mu}{R^{n+2}} \sqrt{\frac{2n+1}{n} \frac{s_n \eta_n r_m^{2n+1}}{4\pi \hbar \varepsilon_0}}, \quad (A11)$$

$$\chi = \varepsilon_b \sqrt{12\pi \varepsilon_0 \hbar \eta_1 r_m^3}. \quad (A12)$$

APPENDIX B: GENERAL EQUATIONS OF SYSTEM DYNAMICS

In this section, we present the general equations for the expectation dynamics, from which we can calculate both the dynamical and steady-state results of the populations and high-order correlation functions. Defining the general operator $\hat{O} \equiv (a_N^\dagger)^{r_N}(a_N)^{s_N} \cdots (a_n^\dagger)^{r_n}(a_n)^{s_n} \cdots (a_1^\dagger)^{r_1}(a_1)^{s_1}$, the dynamics of the system can be described by

$$\frac{d\langle \hat{O} \rangle}{dt} = -\sum_{n=1}^N \left[i(s_n - r_n)(\omega_n - \omega) + (s_n + r_n)\frac{\gamma_n}{2} \right] \langle \hat{O} \rangle$$
$$- \sum_{n=1}^N ig_n r_n \langle (a_N^\dagger)^{r_N}(a_N)^{s_N} \cdots (a_n^\dagger)^{r_n-1}(a_n)^{s_n} \cdots (a_1^\dagger)^{r_1}(a_1)^{s_1}\sigma^\dagger \rangle$$
$$+ \sum_{n=1}^N ig_n s_n \langle (a_N^\dagger)^{r_N}(a_N)^{s_N} \cdots (a_n^\dagger)^{r_n}(a_n)^{s_n-1} \cdots (a_1^\dagger)^{r_1}(a_1)^{s_1}\sigma \rangle$$
$$- \frac{i}{\hbar}E_0\chi r_1 \langle (a_N^\dagger)^{r_N}(a_N)^{s_N} \cdots (a_1^\dagger)^{r_1-1}(a_1)^{s_1} \rangle + \frac{i}{\hbar}E_0\chi s_1 \langle (a_N^\dagger)^{r_N}(a_N)^{s_N} \cdots (a_1^\dagger)^{r_1}(a_1)^{s_1-1} \rangle, \quad (B1)$$

$$\frac{d}{dt}\langle \hat{O}\sigma^\dagger \rangle = -\left\{ \sum_{n=1}^N \left[i(s_n - r_n)(\omega_n - \omega) + (s_n + r_n)\frac{\gamma_n}{2} \right] + i(\omega - \omega_x) + \frac{\gamma_x}{2} \right\} \langle \hat{O}\sigma^\dagger \rangle$$
$$- \sum_{n=1}^N ig_n \langle (a_N^\dagger)^{r_N}(a_N)^{s_N} \cdots (a_n^\dagger)^{r_n+1}(a_n)^{s_n} \cdots (a_1^\dagger)^{r_1}(a_1)^{s_1} \rangle$$
$$+ \sum_{n=1}^N i2g_n \langle (a_N^\dagger)^{r_N}(a_N)^{s_N} \cdots (a_n^\dagger)^{r_n+1}(a_n)^{s_n} \cdots (a_1^\dagger)^{r_1}(a_1)^{s_1}\sigma^\dagger\sigma \rangle - \frac{i}{\hbar}\mu E_0 \langle \hat{O} \rangle$$
$$+ \sum_{n=1}^N ig_n s_n \langle (a_N^\dagger)^{r_N}(a_N)^{s_N} \cdots (a_n^\dagger)^{r_n}(a_n)^{s_n-1} \cdots (a_1^\dagger)^{r_1}(a_1)^{s_1}\sigma^\dagger\sigma \rangle + \frac{i}{\hbar}2\mu E_0 \langle \hat{O}\sigma^\dagger\sigma \rangle$$
$$- \frac{i}{\hbar}E_0\chi r_1 \langle (a_N^\dagger)^{r_N}(a_N)^{s_N} \cdots (a_1^\dagger)^{r_1-1}(a_1)^{s_1}\sigma^\dagger \rangle + \frac{i}{\hbar}E_0\chi s_1 \langle (a_N^\dagger)^{r_N}(a_N)^{s_N} \cdots (a_1^\dagger)^{r_1}(a_1)^{s_1-1}\sigma^\dagger \rangle, \quad (B2)$$

$$\frac{d}{dt}\langle\hat{O}\sigma\rangle = -\left\{\sum_{n=1}^{N}\left[i(s_n-r_n)(\omega_n-\omega)+(s_n+r_n)\frac{\gamma_n}{2}\right]+i(\omega_x-\omega)+\frac{\gamma_x}{2}\right\}\langle\hat{O}\sigma\rangle$$

$$+\sum_{n=1}^{N}ig_n\langle(a_N^\dagger)^{r_N}(a_N)^{s_N}\cdots(a_n^\dagger)^{r_n}(a_n)^{s_n+1}\cdots(a_1^\dagger)^{r_1}(a_1)^{s_1}\rangle$$

$$-\sum_{n=1}^{N}i2g_n\langle(a_N^\dagger)^{r_N}(a_N)^{s_N}\cdots(a_n^\dagger)^{r_n}(a_n)^{s_n+1}\cdots(a_1^\dagger)^{r_1}(a_1)^{s_1}\sigma^\dagger\sigma\rangle+\frac{i}{\hbar}\mu E_0\langle\hat{O}\rangle$$

$$-\sum_{n=1}^{N}ig_nr_n\langle(a_N^\dagger)^{r_N}(a_N)^{s_N}\cdots(a_n^\dagger)^{r_n-1}(a_n)^{s_n}\cdots(a_1^\dagger)^{r_1}(a_1)^{s_1}\sigma^\dagger\sigma\rangle-\frac{i}{\hbar}2\mu E_0\langle\hat{O}\sigma^\dagger\sigma\rangle$$

$$-\frac{i}{\hbar}E_0\chi r_1\langle(a_N^\dagger)^{r_N}(a_N)^{s_N}\cdots(a_1^\dagger)^{r_1-1}(a_1)^{s_1}\sigma\rangle+\frac{i}{\hbar}E_0\chi s_1\langle(a_N^\dagger)^{r_N}(a_N)^{s_N}\cdots(a_1^\dagger)^{r_1}(a_1)^{s_1-1}\sigma\rangle, \tag{B3}$$

$$\frac{d}{dt}\langle\hat{O}\sigma^\dagger\sigma\rangle = -\left\{\sum_{n=1}^{N}\left[i(s_n-r_n)(\omega_n-\omega)+(s_n+r_n)\frac{\gamma_n}{2}\right]+\gamma_x\right\}\langle\hat{O}\sigma^\dagger\sigma\rangle$$

$$+\sum_{n=1}^{N}ig_n\langle(a_N^\dagger)^{r_N}(a_N)^{s_N}\cdots(a_n^\dagger)^{r_n}(a_n)^{s_n+1}\cdots(a_1^\dagger)^{r_1}(a_1)^{s_1}\sigma^\dagger\rangle+\frac{i}{\hbar}\mu E_0\langle\hat{O}\sigma^\dagger\rangle$$

$$-\sum_{n=1}^{N}ig_n\langle(a_N^\dagger)^{r_N}(a_N)^{s_N}\cdots(a_n^\dagger)^{r_n+1}(a_n)^{s_n}\cdots(a_1^\dagger)^{r_1}(a_1)^{s_1}\sigma\rangle-\frac{i}{\hbar}\mu E_0\langle\hat{O}\sigma\rangle$$

$$-\frac{i}{\hbar}E_0\chi r_1\langle(a_N^\dagger)^{r_N}(a_N)^{s_N}\cdots(a_1^\dagger)^{r_1-1}(a_1)^{s_1}\sigma^\dagger\sigma\rangle+\frac{i}{\hbar}E_0\chi s_1\langle(a_N^\dagger)^{r_N}(a_N)^{s_N}\cdots(a_1^\dagger)^{r_1}(a_1)^{s_1-1}\sigma^\dagger\sigma\rangle. \tag{B4}$$

Note that the expectations above are calculated in the rotating frame. The results in the Schrödinger picture can be obtained as follows:

$$\langle\hat{O}\rangle_S = \langle\hat{O}\rangle e^{i\sum_{n=1}^{N}(r_n-s_n)\omega t}, \quad \langle\hat{O}\sigma^\dagger\rangle_S = \langle\hat{O}\sigma^\dagger\rangle e^{i[1+\sum_{n=1}^{N}(r_n-s_n)]\omega t},$$

$$\langle\hat{O}\sigma\rangle_S = \langle\hat{O}\sigma\rangle e^{i[-1+\sum_{n=1}^{N}(r_n-s_n)]\omega t}, \quad \langle\hat{O}\sigma^\dagger\sigma\rangle_S = \langle\hat{O}\sigma^\dagger\sigma\rangle e^{i\sum_{n=1}^{N}(r_n-s_n)\omega t}. \tag{B5}$$

APPENDIX C: DERIVATION OF EFFECTIVE HAMILTONIAN

In this section, we derive the effective Hamiltonian by adiabatically eliminating the higher-mode operators. The derivation here has referred the elimination of the excited state of a two-level atom in Ref. [56]. We begin with the Heisenberg equations of motion for σ and a_n:

$$\dot{\sigma} = -\left[i(\omega_x-\omega)+\frac{\gamma_x}{2}\right]\sigma - \sum_{n=1}^{N}ig_n\sigma_z a_n - i\mu E_0\sigma_z, \tag{C1a}$$

$$\dot{a}_n = -\left[i(\omega_n-\omega)+\frac{\gamma_n}{2}\right]a_n + ig_n\sigma \quad (n\geqslant 2), \tag{C1b}$$

with $\sigma_z = \sigma^\dagger\sigma - \sigma\sigma^\dagger$. These two equations can be formally integrated to give

$$\sigma(t) = \sigma(t_0)e^{-[i(\omega_x-\omega)+\frac{\gamma_x}{2}](t-t_0)} + e^{-[i(\omega_x-\omega)+\frac{\gamma_x}{2}]t}\int_{t_0}^{t}d\tau\left[-\sum_{n=1}^{N}ig_n\sigma_z(\tau)a_n(\tau)-i\mu E_0\sigma_z(\tau)\right]e^{[i(\omega_x-\omega)+\frac{\gamma_x}{2}]\tau}, \tag{C2a}$$

$$a_n(t) = a_n(t_0)e^{-[i(\omega_n-\omega)+\frac{\gamma_n}{2}](t-t_0)} + e^{-[i(\omega_n-\omega)+\frac{\gamma_n}{2}]t}\int_{t_0}^{t}d\tau ig_n\sigma(\tau)e^{[i(\omega_n-\omega)+\frac{\gamma_n}{2}]\tau} \quad (n\geqslant 2). \tag{C2b}$$

By changing the integration variable, we rewrite the above two equations in the form

$$\sigma(t) = \sigma(t_0)e^{-[i(\omega_x-\omega)+\frac{\gamma_x}{2}](t-t_0)} + \int_0^{t-t_0}d\tau\left[-\sum_{n=1}^{N}ig_n\sigma_z(t-\tau)a_n(t-\tau)-i\mu E_0\sigma_z(t-\tau)\right]e^{-[i(\omega_x-\omega)+\frac{\gamma_x}{2}]\tau}, \tag{C3a}$$

$$a_n(t) = a_n(t_0)e^{-[i(\omega_n-\omega)+\frac{\gamma_n}{2}](t-t_0)} + \int_0^{t-t_0}d\tau ig_n\sigma(t-\tau)e^{-[i(\omega_n-\omega)+\frac{\gamma_n}{2}]\tau} \quad (n\geqslant 2). \tag{C3b}$$

We now replace t with $t - \tau$ in Eq. (C3a) and obtain

$$\sigma(t - \tau) = \sigma(t_0)e^{-[i(\omega_x - \omega) + \frac{\gamma_x}{2}](t - \tau - t_0)}$$
$$+ \int_0^{t - \tau - t_0} d\tau' \left[-\sum_{n=1}^{N} ig_n \sigma_z(t - \tau - \tau')a_n(t - \tau - \tau') - i\mu E_0 \sigma_z(t - \tau - \tau') \right] e^{-[i(\omega_x - \omega) + \frac{\gamma_x}{2}]\tau'}. \quad (C4)$$

As t_0 in Eq. (C2a) is arbitrary, so Eq. (C4) holds for $t_0 = t$. Setting t_0 to t in the above expression yields

$$\sigma(t - \tau) = \sigma(t)e^{[i(\omega_x - \omega) + \frac{\gamma_x}{2}]\tau}$$
$$+ \int_{-\tau}^{0} d\tau' \left[\sum_{n=1}^{N} ig_n \sigma_z(t - \tau - \tau')a_n(t - \tau - \tau') + i\mu E_0 \sigma_z(t - \tau - \tau') \right] e^{-[i(\omega_x - \omega) + \frac{\gamma_x}{2}]\tau'}. \quad (C5)$$

Substituting Eq. (C5) into Eq. (C3b) leads to the result

$$a_n(t) = a_n(t_0)e^{-[i(\omega_n - \omega) + \frac{\gamma_n}{2}](t - t_0)} + ig_n \int_0^{t - t_0} d\tau\, e^{-[i(\omega_n - \omega) + \frac{\gamma_n}{2}]\tau} \left\{ \sigma(t)e^{[i(\omega_x - \omega) + \frac{\gamma_x}{2}]\tau} \right.$$

$$\left. + \int_{-\tau}^{0} d\tau'\, e^{-[i(\omega_x - \omega) + \frac{\gamma_x}{2}]\tau'} \left[\sum_{n=1}^{N} ig_n \sigma_z(t - \tau - \tau')a_n(t - \tau - \tau') + i\mu E_0 \sigma_z(t - \tau - \tau') \right] \right\} \quad (n \geqslant 2). \quad (C6)$$

Integrating the above equation by parts, we finally obtain

$$a_n(t) = a_n(t_0)e^{-[i(\omega_n - \omega) + \frac{\gamma_n}{2}](t - t_0)} + \frac{ig_n}{i(\omega_n - \omega_x) + (\gamma_n - \gamma_x)/2}\sigma(t) - \frac{ig_n}{i(\omega_n - \omega_x) + (\gamma_n - \gamma_x)/2}e^{-[i(\omega_n - \omega_x) + (\gamma_n - \gamma_x)/2](t - t_0)}$$

$$\times \left\{ \sigma(t) + \int_{t_0 - t}^{0} d\tau'\, e^{-[i(\omega_x - \omega) + \gamma_x/2](t - t_0 + \tau')} \left[\sum_{n=1}^{N} ig_n \sigma_z(t_0 - \tau')a_n(t_0 - \tau') + i\mu E_0 \sigma_z(t_0 - \tau') \right] \right\}$$

$$+ \frac{ig_n}{i(\omega_n - \omega_x) + (\gamma_n - \gamma_x)/2} \int_0^{t - t_0} d\tau\, e^{-[i(\omega_n - \omega_x) + (\gamma_n - \gamma_x)/2]\tau} \frac{d}{d\tau} \left\{ \int_{-\tau}^{0} d\tau'\, e^{-[i(\omega_x - \omega) + \gamma_x/2](\tau + \tau')} \right.$$

$$\left. \times \left[\sum_{n=1}^{N} ig_n \sigma_z(t - \tau - \tau')a_n(t - \tau - \tau') + i\mu E_0 \sigma_z(t - \tau - \tau') \right] \right\} \quad (n \geqslant 2). \quad (C7)$$

All of the above derivations are exact. As discussed in the main text, to obtain better control of the quantum statistics, the QE transition frequency is set off resonance with the higher modes of MNP. Moreover, the coupling between the QE and MNP is in the bad-cavity limit. As an approximation, we retain first-order terms with respect to $\frac{g_n}{i(\omega_n - \omega_x) + (\gamma_n - \gamma_x)/2}$ only, and drop the fast rotating and decay terms. We now arrive at

$$a_n(t) \approx \frac{ig_n}{i(\omega_n - \omega_x) + (\gamma_n - \gamma_x)/2}\sigma(t) \quad (n \geqslant 2). \quad (C8)$$

Inserting the above expression back into Eq. (C1a), we get

$$\dot{\sigma} = -\left[i(\omega_x - \omega) + \frac{\gamma_x}{2} \right]\sigma - ig_1\sigma_z a_1 - \sum_{n=2}^{N} ig_n \frac{ig_n}{i(\omega_n - \omega_x) + (\gamma_n - \gamma_x)/2}\sigma_z\sigma - i\mu E_0 \sigma_z$$

$$= -\left\{ i\left[\omega_x - \sum_{n=2}^{N} \alpha_n(\omega_n - \omega_x) - \omega \right] + \left[\frac{\gamma_x}{2} + \frac{1}{2}\sum_{n=2}^{N} \alpha_n(\gamma_n - \gamma_x) \right] \right\}\sigma - ig_1\sigma_z a_1 - i\mu E_0 \sigma_z, \quad (C9)$$

where $\alpha_n = \frac{g_n^2}{(\omega_n - \omega_x)^2 + (\gamma_n - \gamma_x)^2/4}$. We have used the relation $\sigma_z\sigma = -\sigma$ in the above derivation. Combining Eq. (C9) with the Heisenberg equation of a_1,

$$\dot{a}_1 = -\left[i(\omega_1 - \omega) + \frac{\gamma_1}{2} \right]a_1 + ig_1\sigma + iE_0\chi, \quad (C10)$$

we then arrive at the effective Hamiltonian [Eq. (7)] and master equation [Eq. (8)] in the main text.

[1] M. Kira and S. W. Koch, Phys. Rev. A **73**, 013813 (2006).

[2] S. W. Koch, M. Kira, G. Khitrova, and H. M. Gibbs, Nat. Mater. **5**, 523 (2006).

[3] M. Kira, S. W. Koch, R. P. Smith, A. E. Hunter, and S. T. Cundiff, Nat. Phys. **7**, 799 (2011).

[4] A. Carmele, A. Knorr, and M. Richter, Phys. Rev. B **79**, 035316 (2009).

[5] M. Mootz, M. Kira, S. W. Koch, A. E. Almand-Hunter, and S. T. Cundiff, Phys. Rev. B **89**, 155301 (2014).

[6] A. Imamoğlu, H. Schmidt, G. Woods, and M. Deutsch, Phys. Rev. Lett. **79**, 1467 (1997).

[7] S. Rebić, A. S. Parkins, and S. M. Tan, Phys. Rev. A **65**, 063804 (2002).

[8] K. M. Birnbaum, A. Boca, R. Miller, A. D. Boozer, T. E. Northup, and H. J. Kimble, Nature (London) **436**, 87 (2005).

[9] A. Faraon, I. Fushman, D. Englund, N. Stoltz, P. Petroff, and J. Vučković, Nat. Phys. **4**, 859 (2008).

[10] A. Majumdar, M. Bajcsy, and J. Vučković, Phys. Rev. A **85**, 041801(R) (2012).

[11] A. Reinhard, T. Volz, M. Winger, A. Badolato, K. J. Hennessy, E. L. Hu, and A. Imamoğlu, Nat. Photon. **6**, 93 (2012).

[12] J. A. Souza, E. Figueroa, H. Chibani, C. J. Villas-Boas, and G. Rempe, Phys. Rev. Lett. **111**, 113602 (2013).

[13] W. L. Barnes, A. Dereux, and T. W. Ebbesen, Nature (London) **424**, 824 (2003).

[14] S. A. Maier, *Plasmonics: Fundamentals and Applications* (Springer, New York, 2007).

[15] O. Benson, Nature (London) **480**, 193 (2011).

[16] M. S. Tame, K. R. McEnery, S. K. Ozdemir, J. Lee, S. A. Maier, and M. S. Kim, Nat. Phys. **9**, 329 (2013).

[17] W. Zhang, A. O. Govorov, and G. W. Bryant, Phys. Rev. Lett. **97**, 146804 (2006).

[18] A. Ridolfo, O. DiStefano, N. Fina, R. Saija, and S. Savasta, Phys. Rev. Lett. **105**, 263601 (2010).

[19] V. Yannopapas, E. Paspalakis, and N. V. Vitanov, Phys. Rev. Lett. **103**, 063602 (2009).

[20] V. Yannopapas and N. V. Vitanov, J. Phys.: Condens. Matter **19**, 096210 (2007).

[21] D. J. Bergman and M. I. Stockman, Phys. Rev. Lett. **90**, 027402 (2003).

[22] M. A. Noginov, G. Zhu, A. M. Belgrave, R. Bakker, V. M. Shalaev, E. E. Narimanov, S. Stout, E. Herz, T. Suteewong, and U. Wiesner, Nature (London) **460**, 1110 (2009).

[23] K. E. Dorfman, P. K. Jha, D. V. Voronine, P. Genevet, F. Capasso, and M. O. Scully, Phys. Rev. Lett. **111**, 043601 (2013).

[24] Y. Osaka, N. Yokoshi, M. Nakatani, and H. Ishihara, Phys. Rev. Lett. **112**, 133601 (2014).

[25] X.-W. Chen, V. Sandoghdar, and M. Agio, Phys. Rev. Lett. **110**, 153605 (2013).

[26] D. Martín-Cano, H. R. Haakh, K. Murr, and M. Agio, Phys. Rev. Lett. **113**, 263605 (2014).

[27] R. D. Artuso, G. W. Bryant, A. Garcia-Etxarri, and J. Aizpurua, Phys. Rev. B **83**, 235406 (2011).

[28] K. Słowik, R. Filter, J. Straubel, F. Lederer, and C. Rockstuhl, Phys. Rev. B **88**, 195414 (2013).

[29] C. F. Bohren and D. R. Huffman, *Absorption and Scattering of Light by Small Particles* (Wiley, New York, 1983).

[30] P. B. Johnson and R. W. Christy, Phys. Rev. B **6**, 4370 (1972).

[31] M. Liu, T.-W. Lee, S. K. Gray, P. Guyot-Sionnest, and M. Pelton, Phys. Rev. Lett. **102**, 107401 (2009).

[32] J. A. Fan, C. Wu, K. Bao, J. Bao, R. Bardhan, N. J. Halas, V. N. Manoharan, P. Nordlander, G. Shvets, and F. Capasso, Science **328**, 1135 (2010).

[33] A. Delga, J. Feist, J. Bravo-Abad, and F. J. Garcia-Vidal, Phys. Rev. Lett. **112**, 253601 (2014).

[34] R. Esteban, J. Aizpurua, and G. W. Bryant, New J. Phys. **16**, 013052 (2014).

[35] J. R. Johansson, P. D. Nation, and F. Nori, Comput. Phys. Commun. **183**, 1760 (2012).

[36] J. R. Johansson, P. D. Nation, and F. Nori, Comput. Phys. Commun. **184**, 1234 (2013).

[37] J.-Y. Yan, W. Zhang, S. Duan, X.-G. Zhao, and A. O. Govorov, Phys. Rev. B **77**, 165301 (2008).

[38] P. Anger, P. Bharadwaj, and L. Novotny, Phys. Rev. Lett. **96**, 113002 (2006).

[39] S. Lal, S. Link, and N. J. Halas, Nat. Photon. **1**, 641 (2007).

[40] K. M. Mayer and J. H. Hafner, Chem. Rev. **111**, 3828 (2011).

[41] M. I. Stockman, Science **348**, 287 (2015).

[42] K. P. Nayak, P. N. Melentiev, M. Morinaga, F. L. Kien, V. I. Balykin, and K. Hakuta, Opt. Express **15**, 5431 (2007).

[43] L. Novotny and N. van Hulst, Nat. Photon. **5**, 83 (2011).

[44] A. V. Akimov, A. Mukherjee, C. L. Yu, D. E. Chang, A. S. Zibrov, P. R. Hemmer, H. Park, and M. D. Lukin, Nature (London) **450**, 402 (2007).

[45] C. Stehle, H. Bender, C. Zimmermann, D. Kern, M. Fleischer, and S. Slama, Nat. Photon. **5**, 494 (2011).

[46] C. Stehle, C. Zimmermann, and S. Slama, Nat. Phys. **10**, 937 (2014).

[47] R. Lettow, Y. L. A. Rezus, A. Renn, G. Zumofen, E. Ikonen, S. Götzinger, and V. Sandoghdar, Phys. Rev. Lett. **104**, 123605 (2010).

[48] D. Leibfried, R. Blatt, C. Monroe, and D. Wineland, Rev. Mod. Phys. **75**, 281 (2003).

[49] Z. Gueroui and A. Libchaber, Phys. Rev. Lett. **93**, 166108 (2004).

[50] Z. Nie, A. Petukhova, and E. Kumacheva, Nat. Nanotechnol. **5**, 15 (2010).

[51] R. Schreiber, J. Do, E.-M. Roller, T. Zhang, V. J. Schüller, P. C. Nickels, J. Feldmann, and T. Liedl, Nat. Nanotechnol. **9**, 74 (2014).

[52] R. H. Brown and R. Q. Twiss, Nature (London) **177**, 27 (1956).

[53] R. H. Brown and R. Q. Twiss, Nature (London) **178**, 1046 (1956).

[54] D. Zhao, Y. Gu, J. Wu, J. Zhang, T. Zhang, B. D. Gerardot, and Q. Gong, Phys. Rev. B **89**, 245433 (2014).

[55] D. Zhao, J. Wu, Y. Gu, and Q. Gong, Appl. Phys. Lett. **105**, 111112 (2014).

[56] S. A. Gardiner, Ph.D. thesis, Leopold-Franzens-Universität Innsbruck, 2000.